Three-Dimensional Localization of Immunogold Markers Using Two Tilted Electron Microscope Recordings

J. P. Pascual Starink,*‡ Bruno M. Humbel,‡ and Arie J. Verkleij‡

*Department of Electrical Engineering, Delft University of Technology, 2626 CD Delft, The Netherlands, and ‡Department of Molecular Cell Biology, Utrecht University, 3584 CH Utrecht, The Netherlands

ABSTRACT A method is presented to determine the three-dimensional positions of immuno-labeled gold markers from tilted electron micrograph recordings by using image processing techniques. The method consists of three basic modules: localization of the markers in the recordings, estimation of the motion parameters, and matching corresponding markers between the views. Localization consists of a segmentation step based on edge detection and region growing. It also allows for the separation of (visually) aggregated markers. Initial estimates for the motion parameters are obtained from a small number of user-indicated correspondences. A matching algorithm based on simulated annealing is used to find corresponding markers. With the resulting mapping, the motion parameters are updated and used in a new matching step, etc. Once the parameters are stable, the marker depths are retrieved. The developed method has been applied to semithin resin sections of A431 cells labeled for DNA and detected by silver-enhanced ultrasmall gold particles. It represents a reliable method to analyze the three-dimensional distribution of gold markers in electron microscope samples.

INTRODUCTION

Many cellular processes and structures can be understood and studied better when three-dimensional (3D) information is available. Therefore, localization of cellular components in both space and time is an important methodology in cell biology. The introduction of electron microscope marker systems, especially colloidal gold particles, revolutionized the power of electron microscopy. A micrograph no longer only illustrates the morphology of a cell, but it also shows the location of biological relevant macromolecules. Thus biochemical data, the reaction catalized by a macromolecule, can be correlated with morphological data, revealing the place in the cell where this reaction takes place. There are specific probes for all types of cellular macromolecules: proteins, lipids, carbohydrates, and nucleic acids (cf. Horisberger, 1992, for a review). The only limitation is given by the fact that the preservation of the biological fine structure and the antigenic or binding determinant in general oppose each other. For unambiguous identification of the cellular structures, the biological material has to be fixed and embedded optimally. The macromolecule to be identified, however, should not be altered in its conformation and should be unimpeded accessible for the marker. Pre-embedding techniques are often the method of choice if the macromolecule of interest is scarce or very sensitive to the preparation procedure. Additionally, it offers the advantages that the label is present in three dimensions and that it is not restricted to the section surface. The macromolecule or its polymers can be followed, and the spatial relationship between the labels and between label and macromolecule, as well as their integration into the cell, can be studied better.

In general, a specimen needs to be sliced to acquire spatial information, either optically or physically. Stacking the sections to reconstruct the object is then necessary, because studying single sections can lead to various kinds of misinterpretation of the 3D structure (Elias, 1971). To reconstruct a graphical representation, one can manually extract the contour of the object in every section, using a digitizer board. The contours are aligned manually either with (Perkins and Green, 1982) or without (Geraud et al., 1988) the help of internal fiducial markers. Manual tracing is time-consuming and represents the limiting step in all 3D reconstruction experiments (Levinthal, 1984). To obtain a pictorial description, one aligns the sections either by hand (Moss et al., 1990) or by use of a computer-sided registration method. The latter method can be based on detected internal feature points (Bron et al., 1990) or on an optimized similarity measure between adjacent images (Venot et al., 1984).

Methods of information recovery from within a section have been developed for light microscopy (Shaw et al., 1989) and electron microscopy but are used mainly in electron microscopy where the depth of field (0.1–2 μm) exceeds the resolving power (3 Å) significantly. Two groups of reconstruction methods are principally used:

1. Tomography. Electron microscope tomography (EMT) is a technique for 3D reconstruction of singular objects from their projection images (Provencher and Vogel, 1988). At least 11 views around the object are needed (Hoppe and Hegerl, 1980). The reconstruction process does not use symmetry information. As a consequence, all specimen and preparation shortcomings will be present in the final 3D reconstruction (Skoglund, 1992).

Received for publication 31 October 1994 and in final form 30 January 1995.

Address reprint requests to Dr. J. P. Pascual Starink, Department of Molecular Biology, Max Planck Institute for Biophysical Chemistry, P.O. Box 2841, 37018 Gottingen, Germany. Tel.: 49-551-201389; Fax: 49-551-201467; E-mail: pascual@mpc175.mpibpc.gwdg.de.

Dr. Starink's current address: Department of Molecular Biology, Max Planck Institute for Biophysical Chemistry, P.O. Box 2841, 37018 Göttingen, Germany.

0006-3495/95/05/2171/10 $2.00

2. Stereo microscopy. This requires two tilted recordings of the section (Peachly, 1986), which are mounted side by side and viewed as a single 3D image (King, 1981). This rapidly produces a 3D presentation of the specimen but suffers from serious limitations (Bonnet et al., 1985): the stereo viewer and the images must be aligned exactly with respect to the orientation of the tilt axis, the stereo angle is limited taking into account the possibilities of modern goniometer stages, and it does not give access to accurate quantitative 3D information.

Quantitative depth information can be obtained by using a parallax bar or a flying spot, for which the tilt axis must be normal to the measurement direction. This is a manual procedure and is very elaborate when processing many points, but because it relies on simple stereological principles it is suitable for (semi-)automatic processing. Attempts in this direction have been made by Bonnet and co-workers, who reconstruct a graphical representation of biological specimens from high-voltage electron microscope stereo views (Bonnet et al., 1985), and by Luther and co-workers, who monitor the collapse of plastic sections when the plastic is irradiated (Luther et al., 1988).

Manual localization of the gold markers in the projected views by using some pointing device such as a digitizer tablet or a mouse is still widely used. Because these locations are used to calculate the depth components of the markers, the disadvantages of this approach are clear: it is biased and poorly reproducible. In this paper we describe a method to localize gold markers accurately in a thick section from (two) tilted transmission electron microscope recordings, using image processing techniques. Immunogold labeling of DNA in interphase nuclei was used as a model system. To challenge the image analysis method further and to be close to routine situation, we used silver-enhanced ultrasmall gold particles as a detection system. Thus high label density was achieved and the particles were partially aggregated.

MATERIALS AND METHODS

The method to retrieve the marker depths can be divided into five steps (Fig. 1). First the markers are localized in the recordings. An initial registration is performed, using the positions of a small number of markers supplied by the user. Then the markers are matched and the model parameters are re-estimated, using the resulting pairs. This procedure is iterated until the model parameters are stable. Finally, the marker depths are retrieved.

Although intermediate results provided, we have tried to keep their adjustment by the user to a minimum at all stages. In particular, the marker positions in the views are preferably not determined manually, because they are closely related to the marker depths and the model parameters.

The methods were implemented in C and linked to the image processing package SCIL-Image (University of Amsterdam, Amsterdam, The Netherlands) on a SUN SPARCstation10. The negatives were recorded by a Sony XC-77CE CCD camera attached to an Imaging Technology VFG frame grabber (Imaging Technology Inc., Woburn, MA) mounted in a PC 486 compatible.

Model

The gold markers are distributed within the section that sits on a grid in the specimen holder. The electron beam projects a bright field image of the specimen onto the image plane, which is defined as the xy plane. The x axis is assumed parallel to the electron beam (the optical axis). The section is tilted about the tilt axis by the tilt angle ϕ. The actual image acquisition is most conveniently done by attaching a camera to the electron microscope and digitizing the signal. However, we chose to photograph the images on 6 cm × 9 cm negatives, to place them on a dazzle light, and to digitize by means of a CCD camera. In this way the region of interest can be chosen afterward, without losing resolution as a result of resampling.

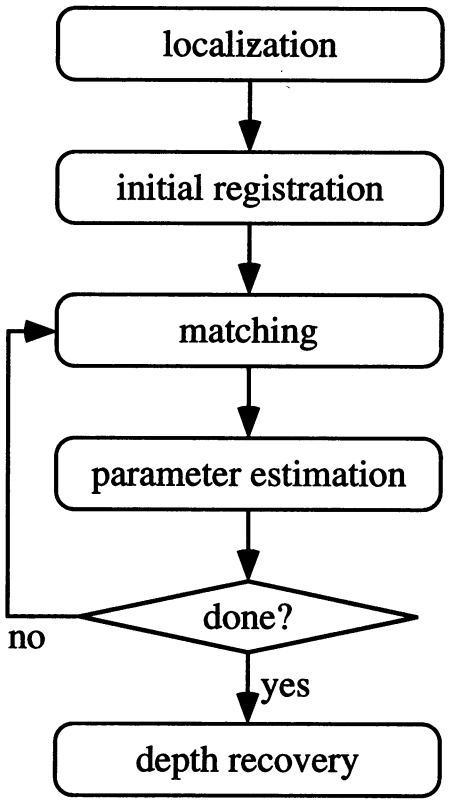

FIGURE 1 Five steps in the method to recover the depth components of the gold markers from tilted electron microscope recordings.

Let the coordinates of the marker centers in 3D space be given by $\mathbf{p}_i$, $i = 1 \ldots N$. Tilting changes coordinates to $\mathbf{p}'_i$, determined by the following geometric operations:

1. Scaling. A scaling difference s between the two recordings is introduced that is due to focusing differences, both in the electron microscope and during digitization of the negatives.

2. Rotation. The specimen is tilted by ϕ about the tilt axis. Furthermore, the electron beam is rotated because of the magnetic forces induced by the microscopes lenses, causing an image rotation by α about the z axis. A rotation by β about the z axis is introduced as a result of misalignment of the negatives during digitization. All these rotations are combined in rotation matrix R.

3. Translation. Relocation of the area of interest after tilting, and a relative shift of the negatives during digitization, cause a translation T in the xy plane.

Because the sections are thin and the opening angle of the electron beam is very small (~0.7°), we assume weak perspective projection instead of perspective projection. This is modeled by a scaling, included in parameter s. The model parameters are combined in an affine transform between the points $\mathbf{p}_i$ and $\mathbf{p}'_i$:

$$\mathbf{p}'_i = s\,R \cdot \mathbf{p}_i + T. \quad (1)$$

Marker localization

Localization of the gold markers is an important step because the positions of the markers are used to estimate the model parameters and consequently

the marker depths. The algorithm we use to find the marker centers is based on recent work (Starink and Young, 1993) and consists of two subsequent steps: segmentation and separation. Before localization, noise peaks are removed (Immi, 1991), and the background, estimated by using circular local max–min filters, is subtracted from the images. The result is smoothed with a Gaussian filter, yielding the image $I(k, l)$.

The segmentation step starts with edge detection by applying a gradient method. We use the ramp version of the Lee detector for a better suppression of nonramp edges (Lee et al., 1986; Verbeek et al., 1988). This filter is based on max–min filters, where the extreme is searched within a circle with radius n centered on (k, l):

$$E(k, l) = \min[\mathrm{LOW}_n(k, l) - \mathrm{MIN}_n(k, l), \mathrm{MAX}_n(k, l) - \mathrm{UP}_n(k, l)], \quad (2)$$

where $\mathrm{LOW}_n(k, l) = \mathrm{MAX}_n[\mathrm{MIN}_n(k, l)]$ and $\mathrm{UP}_n(k, l) = \mathrm{MIN}_n[\mathrm{MAX}_n(k, l)]$.

Region growing (Zucker, 1976; Pavlidis and Liow, 1990) starts by finding kernels with a peak detection algorithm, for which we used the convergent squares algorithm (O'Gorman and Sanderson, 1984). Each neighbor of a kernel is marked "candidates" and is checked against the region-growing criteria (Table 1). If it is a region pixel, it is added to the region, and all unmarked neighbors are marked "candidates." If it is a boundary pixel, it is also added to the region, but all its unmarked neighbors are marked "stop." Based on the response of the smoothing filter (parameter a) and the edge likelihood operator (parameter b), the rule referred to is

$$(k, l) \in \begin{cases} \text{region} & I(k, l) - a/bE(k, l) \le 0 \\ \text{boundary} & \text{otherwise} \end{cases}.$$

Region growing stops when no candidates remain and all kernels have been processed.

The result is an image with regions containing the gold markers. If a region contains only one marker, its center is readily estimated by averaging over the region pixel coordinates. For various reasons such as noise, overprojection, lack of resolution, and abundant staining, the markers may (visually) aggregate. To separate and localize the individual markers, initial estimates for their positions and sizes are determined. Because a marker is approximately round, its inscribing circle, identified by a peak value in the distance image (Borgefors, 1986), serves as an initial estimate. The location of the peak corresponds to the center; its value, to the radius. Usually, more peaks than the number of actually present markers are detected. To yield the most probable peaks, they are selected in descending order of magnitude, and peaks covered by the inscribing circle of a selected peak are removed.

Then all markers, initially the inscribing circles, are dilated simultaneously. If a marker cannot be dilated with pixels not covered by the markers, it is left unchanged. Dilation continues until the region is entirely covered. The new markers are used to update their center positions and radii, which are fed into a new dilation step. This process is iterated until the centers are stable. Three operations allow manual correction of the results:

1. Dark spots resulting from noise or staining may result in untrue markers. These may affect the final result and should be removed.

2. Although it is unwanted, manual localization of undetected markers is supported. This operation can be partially avoided by tuning the region growing parameters such that slightly more markers than actually present are detected. Afterward, the remaining untrue markers can be removed.

TABLE 1 Classification of pixel candidates

	$I(k, l)$		
$E(k, l)$	$[0, a-\sigma_a\rangle$	$[a-\sigma_a, a+\sigma_a]$	$\langle a+\sigma_a, 1]$
$[0, b-\sigma_b\rangle$	Reject	Region	Region
$[b-\sigma_b, b+\sigma_b]$	Boundary	Rule	Region
$\langle b+\sigma_b, 1]$	Boundary	Boundary	Boundary

For both the pixel intensity $I(k, l)$ and the pixel edge likelihood $E(k, l)$, three regions are defined based on the parameters a and b and their standard deviations σ_a and σ_b. Classifications are given for all combinations. The rule referred to is explained in the text.

3. Identifying undetected markers in multimarker regions is done by supplying the separation procedure with points located near the centers of the missing markers.

Model parameters

For parallel and weak perspective projections, the locations and direction of the epipolar lines can be estimated from four correspondences of two views (Lee and Huang, 1990). Thus the user must supply the system with at least the four sure correspondences to perform the initial mapping. To estimate tilt angle ϕ, four correspondences of at least three views are required (Ullman, 1979; Huang and Lee, 1989). When only two views are used in the analysis, the tilt angle must be read from the goniometer stage.

An iterative procedure to estimate the model parameters from two views has been described in Bonnet et al., 1985. A more sophisticated model and a numerical procedure to estimate the parameters from any number of views have been described by Luther et al. (1988). Here we briefly describe a numerical procedure to estimate the parameters in our model using two views, assuming that the tilt axis is parallel to the image plane. First the user-indicated correspondence $(\mathbf{p}_1, \mathbf{p}'_1)$ is used to undo translation T, using relative displacement:

$$\mathbf{p}'_i - \mathbf{p}'_1 = s\,R \cdot \mathbf{p}_i + T - (s\,R \cdot \mathbf{p}_i + T) = s\,R \cdot (\mathbf{p}_i - \mathbf{p}_1). \quad (3)$$

With matrix $R = R_z(\beta) \cdot R_z(\alpha) \cdot R_z(\phi) \cdot R_z(-\alpha)$, the points are corrected for translation and normalized for scaling and rotation in the xy plane:

$$\mathbf{p}_i \leftarrow s\,R_z(-\alpha) \cdot (\mathbf{p}_i - \mathbf{p}_1), \qquad \mathbf{p}'_i \leftarrow R_z(-\alpha-\beta) \cdot (\mathbf{p}'_i - \mathbf{p}'_1). \quad (4)$$

By this, the epipolar lines become parallel to the x axis. Now Eq. 1 becomes

$$\mathbf{p}'_i = R_x(\phi) \cdot \mathbf{p}_i. \quad (5)$$

This rotation about the x axis leaves the x coordinate unchanged, so $\mathbf{p}'_{i,x} = \mathbf{p}_{i,x}$:

$$\cos(-\alpha-\beta) \cdot \mathbf{p}'_{i,x} - \sin(-\alpha-\beta) \cdot \mathbf{p}'_{i,y} = s\cos(-\alpha) \cdot \mathbf{p}_{i,x} - s\sin(-\alpha) \cdot \mathbf{p}_{i,y}. \quad (6)$$

This nonlinear system is rewritten as

$$y_i(\mathbf{a}) = \cos(\gamma)\mathbf{p}'_{i,x} + \sin(\gamma)\mathbf{p}'_{i,y} - s\cos(\alpha)\mathbf{p}_{i,x} - s\sin(\alpha)\mathbf{p}_{i,y}, \qquad \mathbf{a} = (\alpha\ \gamma\ s)^t, \quad \gamma = \alpha + \beta. \quad (7)$$

Minimizing $\chi^2 = \Sigma_i y_i^2$ is readily performed with a standard, nonlinear minimization scheme such as the Levenberg–Marquardt method (Vetterling et al., 1993). Finally, the depth component is estimated, using the y coordinate of the normalized coordinates in Eq. 5:

$$\mathbf{p}_{i,z} = s\,\frac{\cos(\phi)\mathbf{p}_{i,y} - \mathbf{p}'_{i,y}}{\sin(\phi)}. \quad (8)$$

The distance $d(\mathbf{p}'_j, \lambda_i)$ of the candidate $\mathbf{p}'_j$ to the epipolar line λ_i of $\mathbf{p}_i$ is given by

$$d(\mathbf{p}'_j, \lambda_i) = |\,\mathbf{p}_{i,x} - \mathbf{p}'_{j,x}\,|. \quad (9)$$

Marker correspondences

In the matching step we have to determine for each marker in the untilted view the corresponding marker in the titled view. Generally, in matching one tries to identify corresponding elements in slightly different views. Depending on the representation of the elements, this can be approached in several ways (Lemmens, 1988). The signal approach treats the images as two-dimensional signals. The elements are usually pixel neighborhoods, which are detected in one image and sought for in the other. The feature approach was introduced by Marr (Marr, 1979). The elements are local objects such as points and edges. They are detected in both images and matched afterward. In the structural approach, structures and their relationships are organized in graphs (Boyer and Kak, 1988), which are matched

by using inexact graph matching (Shapiro and Haralick, 1981). If costs are defined reciprocal to the similarity measures, the minimum cost match corresponds to the optimum match. General approaches to finding this match include linear programming (Ullman, 1979), relaxation labeling (Hummel and Zucker, 1983), simulated annealing (Barnard, 1980), and dynamic programming (Otha and Kanade, 1985).

In our problem the markers, represented by their centers, are the elements in the matching. Inasmuch as both views probably contain a different number of markers, looking for one-to-one correspondences is not sufficient. Therefore a marker is allowed to match either a marker in the other view or the null space. Cost $c(\mathbf{p}_i, \mathbf{p}'_j)$ specifies the pair cost that is charged when $\mathbf{p}_i$ and $\mathbf{p}'_j$ are paired and is a weighted sum of the coefficients $c_k(\mathbf{p}_i, \mathbf{p}'_j)$:

$$c(\mathbf{p}_i, \mathbf{p}'_j) = \sum_k a_k c_k(\mathbf{p}_i, \mathbf{p}'_j), \tag{10}$$

where the coefficients c_k should reflect both general and application-specific properties and features. We describe three such cost coefficients.

Epipolar distance

Although all possible correspondences should be regarded, commonly the candidate lists are reduced by setting an upper boundary on the distance to the epipolar line. Consider the candidates $\mathbf{p}_i$ and $\mathbf{p}'_j$ for matching. The positional error of the epipolar line λ_i is σ_{pos}. If the error is normally distributed, then the positional error of $\mathbf{p}'_j$ relative to λ_i is $\sqrt{2}\sigma_{pos}$. With a probability of 95%, the true correspondence of $\mathbf{p}_i$ is located within distance $d_{max} = 1.96\sqrt{2}\sigma_{pos} \approx 2.8\,\sigma_{pos}$ of the epipolar line. The cost coefficient is now defined as the squared epipolar distance when it is smaller than d_{max} and as $+\infty$ otherwise. It is set to $1.2\,d^2_{max}$ when either candidate is null:

$$c_1(\mathbf{p}_i, \mathbf{p}'_j) = \begin{cases} d(\mathbf{p}'_j, \lambda_i)^2 & d(\mathbf{p}'_j, \lambda_i) < d_{max} \\ +\infty & d(\mathbf{s}'_p, \lambda_i) \geq d_{max} \\ 1.2\,d^2_{max} & p_i = 0 \text{ or } p'_j = 0 \end{cases}. \tag{11}$$

Gray-value correlation

The gray-value correlation between the neighborhoods of the marker centers is used to define another cost coefficient. The correlation coefficient $r(\mathbf{p}_i, \mathbf{p}_j)$ between the two regions surrounding the candidates, corrected for scale changes in gray-value amplitude as defined in Gonzales and Wints (1987) lies between −1 and 1, ranging from noncorrelation to perfect correlation. The second cost coefficient is now defined as $c_2(\mathbf{p}_i, \mathbf{p}'_j) = 1 - r(\mathbf{p}_i, \mathbf{p}'_j)$.

Layout similarity

The third cost coefficient is based on the layout configuration between the candidates' closest neighbors. First the n nearest points to $\mathbf{p}_i$ are collected as $\mathbf{s}_k$, $k = 1 \ldots n$. Assume that $\mathbf{s}_{k,z} = \mathbf{p}_{i,z}$, than with Eq. 8 the expected position of these neighbors is $\hat{\mathbf{s}}'_k$, where $\hat{\mathbf{s}}'_{k,x} = \mathbf{s}_{k,x}$ and $\hat{\mathbf{s}}'_{k,y} = \mathbf{p}'_{i,y} + \cos(\phi)(s_{k,y} - \mathbf{p}_{i,y})$. If the two points $\mathbf{p}_i$ and $\mathbf{p}'_j$ are a true correspondence, then the true counterpart of each $\mathbf{s}_k$ should be located near its expected position. This is examined by matching each $\hat{\mathbf{s}}'_k$ to the set of tilted markers. The cost matrix is of size $n \times N'$. The pair cost c^* is defined as a weighted sum of the squared distance to the epipolar line (Eq. 11) and the distance between the candidates along the epipolar line:

$$c^*(\mathbf{s}_k, \mathbf{p}'_j) = a^*_1 c_1(\mathbf{s}_k, \mathbf{p}'_j) + a^*_2 |\hat{\mathbf{s}}'_{k,y} - \mathbf{p}'_{j,y}|.$$

This matching problem is solved with a simple best-first scheme: Repeat selecting the minimum cost pair until at least one set is empty. The cost coefficient c_3 is now the mapping cost of the n matched points.

The method that we present here to generate the (close to) minimum cost mapping between the markers in the two views is based on simulated annealing (Starink, 1995). Simulated annealing is a stochastic optimization algorithm based on the physical analogy of annealing a system of molecules to its ground state. To bring a synthetic system to equilibrium, the cooling process is simulated by the standard method of Metropolis et al. (1953). The rate of cooling must be slow enough so that the system does not get stuck in local minima. Originally developed by Kirkpatrick et al. (1983), the method has been applied to a variety of hard optimization problems (El Garnal et al., 1987; Černý, 1985; Carnevali et al., 1985; Tan and Gelfland, 1992; and Barnard, 1986).

We are given the finite set $\mathcal{M}$ of all possible mappings and the cost (energy) function $E(\mathcal{M})$, which is the sum of all pair costs. The probability of occurrence of any particular mapping $\mathbf{m}$ is proportional to its Boltzmann weight, $\mathrm{P}[\mathbf{m}] \propto \exp(E(\mathbf{m})/T)$. For each state $\mathbf{m} \in \mathcal{M}$ there is a set $N(\mathbf{m}) \subset \mathcal{M}$ that contains the neighboring mappings of $\mathbf{m}$. Let $T_i \geq T_2 \geq \ldots$ be a sequence of strictly positive numbers such that $\lim_{k\to\infty} T_k = 0$. With $[X]^+ = \max(X, 0)$, the general form of the annealing algorithm is

Set $k = 0$.
Choose initial mapping $\mathbf{m}_k$
while $T_k \neq 0$ **do**
  Choose a next state $\mathbf{m}'$ from $N(\mathbf{m}_k)$:

$$\text{Set } \mathbf{m}_{k+1} = \begin{cases} \mathbf{m}' & \text{with probability } \exp\left(\frac{-[E(\mathbf{m}') - E(\mathbf{m})]^+}{T_k}\right) \\ \mathbf{m} & \text{otherwise} \end{cases}.$$

  Set $k = k + 1$.
end.

With $\mathcal{M}^*$ the set of globally minimal states, we try to achieve $lim_{k\to\infty} \mathrm{P}[\mathbf{m}_k \in \mathcal{M}^*] = 1$ by letting T_k tend to zero as k leans to infinity. Asymptotic convergence in this probability is reached only if

$$\sum_{k=1}^{\infty} \exp\left(\frac{-d^*}{T_k}\right) = +\infty, \tag{12}$$

where d^* is the maximum of depths of local minima (Geman and Geman, 1984; Hajek, 1988). If the temperature schedule assumes the parametric form $T_k = c/\log(k + 1)$, this is true when $c \geq d^*$.

To apply this scheme, first an initial mapping is generated, using the best-first approach described above. Remaining unmatched points are matched to null. Parameter c is set to the maximum pair cost in the initial mapping. Although this value is probably too high, it proves to be an adequate guess. Now define a rearrangement as a change in the mapping such that the two candidates $\mathbf{p}_i$ and $\mathbf{p}'_j$ become a pair and the new mapping is part of $N(\mathbf{m})$. The candidates are randomized, and one of them may be null. If the change in energy ΔE resulting from the rearrangement is negative, the rearrangement is accepted; otherwise it is accepted with a chance according to the Boltzmann probability distribution.

Allowing candidates to match either null (unmatched) or another point gives rise to six different configurations. The rearrangements are illustrated in Fig. 2. The configurations left of the arrows represent the situation before, the configuration right of the arrows the situation after the rearrangements. The candidates are gray, $\mathbf{p}_i$ in the left sets, and $\mathbf{p}'_j$ in the right sets. Null is drawn as a circle on top of the sets.

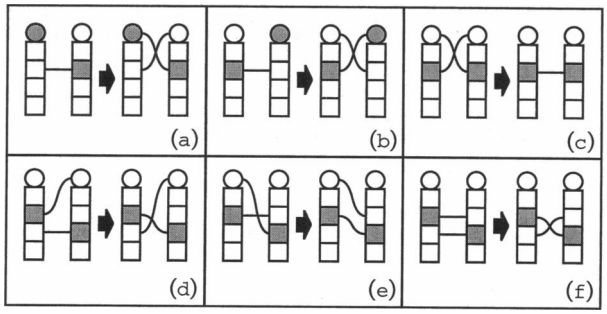

FIGURE 2 Rearrangements of the randomized configurations. Six different configurations can occur (left of the arrows), which are rearranged such that a legal configuration results (right of the arrows). (*a*)–(*f*), Related energy changes as described in Eq. 13.

The energy changes related to the six rearrangements are

$$\Delta E = -2c(\bar{\mathbf{p}}'_j, \mathbf{p}'_j) + c(\bar{\mathbf{p}}'_j, 0) + c(0, \mathbf{p}'_j), \quad (13a)$$

$$\Delta E = -2c(\mathbf{p}_i, \bar{\mathbf{p}}_i) + c(\mathbf{p}_i, 0) + c(0, \bar{\mathbf{p}}_i), \quad (13b)$$

$$\Delta E = -c(\mathbf{p}_i, 0) - c(0, \mathbf{p}'_j) + 2c(\mathbf{p}_i, \mathbf{p}'_j), \quad (13c)$$

$$\Delta E = -c(\mathbf{p}_i, 0) - c(\bar{\mathbf{p}}'_j, \mathbf{p}'_j) + c(\mathbf{p}_i, \mathbf{p}'_j) + c(\bar{\mathbf{p}}'_j, 0), \quad (13d)$$

$$\Delta E = -c(\mathbf{p}_i, \bar{\mathbf{p}}_i) - c(0, \mathbf{p}'_j) + c(\mathbf{p}_i, \mathbf{p}'_j) + c(0, \bar{\mathbf{p}}_i), \quad (13e)$$

$$\Delta E = -c(\mathbf{p}_i, \bar{\mathbf{p}}_i) - c(\bar{\mathbf{p}}'_j, \mathbf{p}'_j) + c(\mathbf{p}_i, \mathbf{p}'_j) + c(\bar{\mathbf{p}}_i, \bar{\mathbf{p}}'_j), \quad (13f)$$

where 0 corresponds to a null candidate and where the points that are matched to the candidates are denoted by $\bar{\mathbf{p}}_i$ and $\bar{\mathbf{p}}'_j$.

Rearrangements are randomized until, theoretically, the temperature is zero. But, because the temperature will never reach zero, the following stop criterion is used. At first, the mapping will change rapidly to lower-energy mappings. Later, as temperature decreases or when the minimum cost mapping is approached, the rate of accepted changes toward higher-cost mappings will steadily increase until it approximates the rate of changes to lower-cost mappings. A reasonable test for equilibrium is when the ratio of changes to higher- and changes to lower-cost mappings, as measured over a fixed number of accepted rearrangements, is stable.

Specimen preparation

The methods described in the previous sections were developed for general use in 3D marker localization. We have quantified the method using A431 epidermoid carcinoma cells. The cells were grown in Dulbecco's modified eagle's medium supplemented with 7.5% (v/v) fetal calf serum in a humidified atmosphere at 7% CO_2 and 37°C. They were seeded on Thermanox cover slips (LUX, Naperville, IL) and grown to a density of 50%–60% confluency. The cells were washed with PBS (pH 7.4), prefixed with 0.25% (v/v) acrolein in PBS, and permeabilized with 0.5% (w/v) Triton X-100 in a cytoskeleton buffer (CSK, 100-mM NaCl, 300-mM sucrose, 3-mM $MgCl_2$, 1-mM ethylene glycol-*bis*(β-aminoethyl ether) *N,N,N',N'*-tetraacetic acid, 1.2-mM phenylmethylsulfonyl fluoride, 10-mM piperasine-*N,N'-bis*[2-ethanesulfonic acid], pH 6.8) (Fey et al., 1986) for 5 minutes at room temperature. The cytoskeleton preparations were fixed with 2% (w/v) formaldehyde and 0.02% (v/v) glutaraldehyde in PBS. They were labeled with a primary antibody against DNA (gift of Dr. R. Smeenk, The Netherlands Red Cross blood transfusion service, Amsterdam, The Netherlands) and a secondary ultrasmall gold-tagged antibody. The ultrasmall gold particles were enlarged with silver enhancing according to the method of Denscher (1981) for 25 min at 20°C. The preparations were cryoprotected with 30% (v/v) dimethylformamide in bidistilled water (Meissner and Schwarz, 1990) and frozen in a cryofixation system KF80 (Reichert-Jung, Wien, Austria) by plunging. The samples were dehydrated with methanol containing 0.5% (w/v) uranylacetate by freeze substitution (Humbel and Müller, 1986) and embedded in Epon. Sections of ~250-nm thickness were cut parallel to the substrate. The sections were irradiated in the electron beam for a few minutes prior to taking pictures were taken. Thus blurring and loss of resolution owing to the initial collapsing may be avoided (Luther et al., 1988).

EXPERIMENTAL RESULTS

In this section we discuss the accuracy of the localization method and the matching method as determined from model data. A practical study on A431 cells is presented.

Localization

The region growing procedure depends on the two parameters a and b, where a is related to the gray-value range of the internal pixels and b to the gray-value range of the edge pixels. In Starink (1993) these parameters were determined experimentally for different edge types and for a broad range of the signal-to-noise ratio as $a \approx 0.6 \pm 0.1$ and $b \approx 0.3 \pm 0.1$.

Also in Starink (1993) the localization error was determined experimentally. Here, convex objects of 15 pixels in size were used to construct one-, two-, and three-marker regions with nonoverlapping centers. The localization error was determined, again over a broad noise range (Fig. 3). Under regular conditions, the localization error proves to be smaller than 0.5 pixel and approaches 1.0 only for very low signal-to-noise ratios (~1.0).

Matching

An experiment was performed to determine the rate of convergence of the matching algorithm. As a model system, 100 points were randomly distributed in a 100 × 100 × 50 rectangular space, rotated over 30° around the x axis and projected onto the xy plane. We displaced these points by adding a normally distributed, zero mean vector. The initial mapping was constructed by matching all the points in both sets to null. Pair costs were calculated by using the squared epipolar distance (weight 0.75) and five-neighbor layout similarity (weight 0.25). Parameter c in the temperature schedule was set to the difference between the minimum and the maximum pair costs in the initial mapping.

Fig. 4 *a* shows that smaller positional errors lead to lower-cost mappings and that the matching algorithm converges faster. The percentage of correctly matched pairs (Fig. 4 *b*) was determined from matching 100 sets.

Practical example

As a practical example, we show a study on A431 epidermoid carcinoma cells, which were prepared as described in the subsection headed Specimen Preparation. Pictures of the specimen were taken in untilted position and at a tilt angle

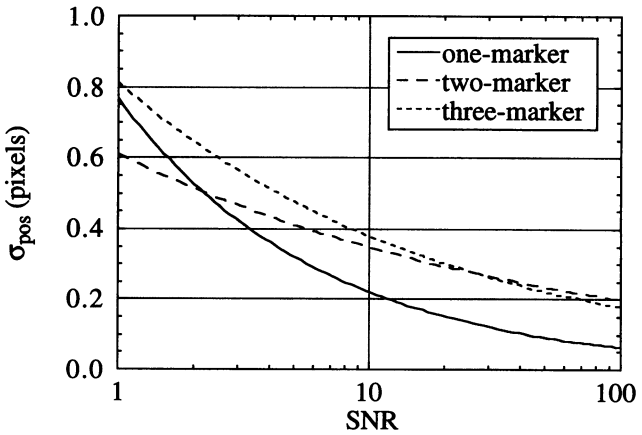

FIGURE 3 Localization error. The positional error σ_{pos} of the localized marker centers in one-, two-, and three-marker regions was determined as a function of the signal-to-noise ratio (SNR). The markers had a surface area of ~15 pixels.

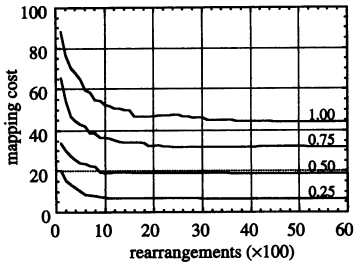

a.

σ_{pos}	correctly matched pairs
0.25	98.1%
0.50	96.0%
0.75	92.6%
1.00	85.3%

b.

FIGURE 4 Convergence of the matching algorithm. In a 100 × 100 × 50 block, 100 points were randomly distributed and tilted about the x axis by 30°. The tilted set was displaced by a normally distributed, zero-mean vector. The mapping cost as a function of the number of rearrangements was determined for σ_{pos} equal to 0.25, 0.50, 0.75 and 1.00 (*a*). Over 100 tests, the mean percentage of correctly matched pairs was calculated (*b*).

of 30° at a magnification of 34,600 in an EM 420 (Philips, Eindhoven, The Netherlands) electron microscope at 120-kV acceleration voltage and were recorded on Agfa Scienta 23D56 sheet films.

The images are shown as pairs; the left image shows the untilted view and the right image shows the tilted view. The original recordings, shown in Fig. 5 *a*, were preprocessed by removing the noise peaks and applying a background subtraction. Fig. 5 *b* shows the segmentation result and Fig. 5 *c* the detected markers overlayed on the original recordings. The initial registration was computed from eight user-supplied correspondences. The result of the matching is shown in Fig. 5 *d* and as two perspective views of the 3D positions of the gold markers in Fig. 5 *e*.

The matching procedure was called three times before the model parameters were stable. The cost coefficients used were the epipolar distance (weight 0.75) and the five-neighbor lay-out similarity (weight 0.25). The tilt angle seemed to be too big to give a useful gray-value cross correlation. Angle α between the x axis and the tilt axis was estimated as 100.9° ± 0.18, rotation β between the two recording as 0.8° ± 0.05, and scaling s as 1.001 ± 0.00.

The localization step resulted in 105 markers in the untilted view and 152 markers in the tilted view. Visual inspection showed that in the untilted view four markers were occluded and nine were not present in the tilted view. In the tilted view nine were occluded, and thirty-six were not present in the untilted view. The simulated annealing loop needed about 9,000 rearrangements to reach convergence. The matching results showed that from the 99 present pairs, the method missed 4 true pairs and made 7 mismatches among the 103 matched pairs, yielding an error of ~6%.

DISCUSSION

An image-processing method is presented to extract three-dimensional (3D) information on thick resin sections of pre-embedding labeled biological specimens. Visualization of the third dimension can be essential to unequivocal allocation of a label to a certain structure or to deciding whether there is colocalization.

At present, pre-embedding techniques need permeabilization of the cell membrane and, to a certain extent, removal of some of the cytoplasmic proteins to guarantee label and marker penetration. There are several methods in use, such as prefixation of the cells and treatment with detergents, such as Triton X-100 (Nickerson et al., 1990; de Graaf et al., 1991) or Sapomin (Burry et al., 1992). Detergent treatment results in a complete loss of lipids and an uncontrolled loss of proteins. Additionally, it favors aggregation of the retained macromolecules. An improved method especially useful to label membrane proteins was introduced by Krijnse-Locker et al. (1994). The plasma membrane is permeabilized with the pore-forming toxin streptolysine O; the intracellular membranes are not affected. Even the targeting mechanism for nuclear proteins remains intact (Downes et al., 1992).

The success of pre-embedding labeling is dependent not only on an adequate permeabilization protocol but also on the size of the marker. Large gold particles cannot pass the barrier of the lamina–pore complex; hence only ultrasmall gold particles could reveal the distribution of an intranuclear antigen (de Graaf et al., 1991). Ultrasmall gold particles may even penetrate into nonpermeabilized, glutaraldehyde fixed PtK2 cells (Leunissen et al., 1989) and into formaldehyde-fixed and borohydride-treated nerve cells (Lookeren-Campagne et al., 1992). Those nondetergent methods would greatly improve the structural preservation and thus give better information about the 3D distribution of a labeled macromolecule. An additional method that is not yet fully exploited is labeling of sections after removal of the embedding material (Nickerson et al., 1990; Baigent and Müller, 1990).

When labeling cytoskeletal proteins, say with 5 or 10-nm markers, the labeling efficiency usually is adequate. The markers are clearly visible, and aggregation stems only from overprojection. These studies and even double-labeling studies can be processed without many difficulties. To label nuclear proteins, ultrasmall gold markers of ~1 nm are needed to penetrate the nucleus. The label density of these small markers is higher for several reasons. The steric hindrance of other gold-tagged antibodies is reduced, and the repulsion between the charged markers is smaller, resulting in a smaller minimum distance between labeled proteins. Additionally, more markers may bind to the secondary antibody. The particles are not visible in electron microscope bright field images, and a silver enhancement step must be used to visualize them. But because the particles are closely spaced, physical aggregation is unavoidable. Furthermore, the ultrasmall particles are not homogeneously sized. They vary from less than 1 nm to 3 nm in size (Otten et al., 1992; Stierhof et al., 1992). The not effect is that in the recordings the markers not show only a large degree of aggregation but also variations in size, which further complicates the localization procedure.

The sections are preferably as thick as possible to maximize the 3D information obtained. This also benefits serial section studies. On the other hand, the number of markers

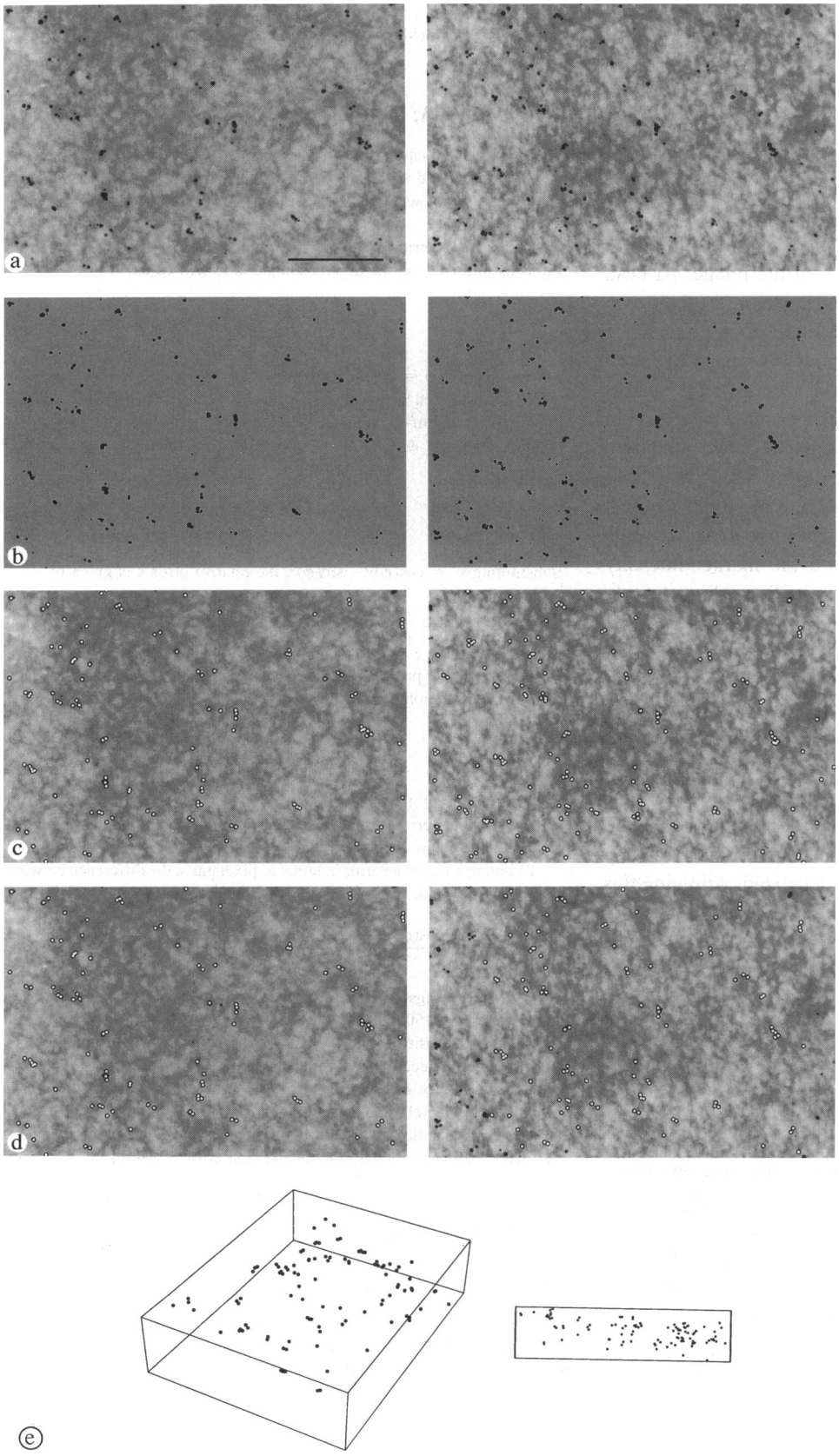

FIGURE 5 Three-dimensional localization of silver enhanced, ultrasmall gold markers, immuno labeled for DNA in A431 cells from two views (0° and 30°). The original recordings (*a*) were segmented into gold regions (*b*). The marker centers were localized (*c*) and matched. Panel (*d*) shows the corresponding markers and panel (*e*) two perspective views of the 3D marker distribution. Original magnification × 34,600. Bar = 150 nm.

increases in thicker sections, resulting in more overprojection hampering localization and matching. Additionally, the contrast decreases and staining will overshadow the markers, again hindering localization. Finally, the lateral resolution

decreases because of the contribution of inelastic scattered electrons. Generally, we are able to process sections of up to ~300 nm and containing more than 300 markers successfully.

The presented method employs the positions of the markers in the projection views. The size of a marker should be approximately 15 pixels to be detected with a satisfactory accuracy. This, of course, depends on the magnification and the sampling resolution. Furthermore, the markers should be clearly distinguishable from the rest of the image. At best, they are the only visible structures. However, on their own they do not supply meaningful information and should be related to biological relevant structures visualized by staining. Denser staining means that it is harder to find the markers, but because the markers are always somewhat darker, a possibility of obtaining a better distinction between the two is to record the specimen twice, one (normal) recording aiming for an optimal stain contrast and the other for an optimal marker contrast by overexposure. By this, the dynamic range of the gray values is moved toward the marker intensity range, which may benefit localization. Recording directly with a slow-scan CCD camera would further add to the quality of the images and thus to the reconstruction method described.

The matching result depends directly on the accuracy of the marker locations, the cost function, and the marker density. High marker density results in more overprojection and, consequently, in more unmatched markers. To deal with the overprojection more efficiently, a marker could be allowed to match any number of markers in the other view. In this way also, overprojected particles can be localized. Allowing this multiple matching increases the matching time slightly but generally generates a better mapping. However, studies showed that allowing a marker to match more than two markers does not necessarily improve the mapping result (Starink, 1995).

The model parameters are estimated from the marker locations in two views of the specimen. The tilt angle in this case is read from the goniometer stage. Although the tilt angle may be estimated from the marker positions in the projection views when three or more tilts are employed (Luther et al., 1988), we have chosen to use only two recordings. By this we save processing time and avoid possible inaccuracy from matching errors. Furthermore, the tilt angle can be read from the goniometer stage quite accurately (error <0.25°). The analysis in Appendix A shows that the effect of an error in the tilt angle on the marker depth may well be below the effect of the localization error on the depth.

In serial section reconstruction, the assumption of the tilt axis being parallel to the image plane may prove to be too strict. Releasing this assumption mainly complicates evaluating the cost function. In the Appendix B we derive an equation for the epipolar distance in case of nonparallel tilting. With it, the cost coefficient of Eq. 11 can be evaluated, and matching can be performed as described.

This work was partially supported by "The Netherlands' Team for Computer Science Research (SPIN)," project "Three-Dimensional Image Analysis."

APPENDIX A: ERROR ANALYSIS

The marker depths are estimated by utilizing the normalized y coordinates of the markers and tilt angle ϕ (Eq. 8). The accuracy of the estimate is determined by the accuracy of the marker localization and by the accuracy of the tilt angle.

The positional error of the markers in the projection views is σ_{pos}. From Eq. 8 its influence on the depth estimate is expressed as

$$\sigma_z = \sqrt{\frac{\cos^2(\phi) + 1}{\sin^2(\phi)}}\,\sigma_{pos}. \tag{14}$$

For example, at $\phi = 40°$, σ_z is about twice the localization error σ_{pos}.

When two tilted views are used, the tilt angle must be read from the goniometer stage of the microscope. Assume that the readout error $\delta\phi$ is additional, so $\hat{\phi} = \phi + \delta\phi$. The z coordinate of a marker is then estimated as

$$\hat{z} = \frac{\cos(\hat{\phi})y - y'}{\sin(\hat{\phi})}. \tag{15}$$

Substituting $y' = \cos(\phi)y - \sin(\phi)z$, the relative error ϵ is given by

$$\epsilon = \frac{\hat{z}_i - z_i}{z_i} = \frac{y_i}{z_i}\frac{\cos(\hat{\phi}) - \cos(\phi)}{\sin(\hat{\phi})} + \frac{\sin(\phi)}{\sin(\hat{\phi})} - 1. \tag{16}$$

Assuming that the particles are uniformly distributed throughout the specimen, the expectation of ϵ with respect to y and z becomes

$$E_{y,z}(\epsilon) = \frac{\sin(\hat{\phi})}{\sin(\phi)} - 1. \tag{17}$$

For example, at 30° tilting and for a readout error of 0.25°, the average error is ~0.75%. The error shows that underestimation of ϕ affects the depth estimate more than overestimation by the same amount.

To obtain an average error in terms of pixel units, the difference between the estimated depth and the real depth is determined:

$$\hat{z} - z = y\frac{\cos(\hat{\phi}) - \cos(\phi)}{\sin(\hat{\phi})} + z\left(\frac{\sin(\phi)}{\sin(\hat{\phi})} - 1\right). \tag{18}$$

Consider recordings of a 250-nm section on 6 cm × 6 cm negatives at a magnification of 150,000. The specimen area imaged is 4 μm × 4 μm, and at a sampling density of 512 × 512 pixels the height would be 64 pixels. The specimen is recorded at two positions, one at 0° and one tilted by 30°. If the readout error $\delta\phi$ is 0.25°, then the average error in the z coordinates would be 0.67 pixel, obtained by integrating Eq. 18 over y and z.

The analysis indicates that a readout error in the tilt angle probably affects the depth estimate less than the localization error σ_{pos} does.

APPENDIX B: NONPARALLEL TILTING

When the assumption that the tilt axis is parallel to the image plane is discarded, the epipolar distance (Eq. 9), and consequently the cost coefficient (Eq. 11) are no longer valid. To derive the epipolar distance, the direction and the locations of the epipolar lines must be estimated from four correspondences of two views, as described in Lee and Huang (1990). For that purpose, the rotation matrix R is written as $R = [r_{ij}]$, $i, j = 1, 2, 3$. Now define

$$\begin{aligned}(r_{13}, r_{23})^t = \eta l_1, \qquad (r_{31}, r_{32})^t = \eta l_2, (-r_{23}, r_{13})^t \\ = \eta l_1^*, \qquad (r_{32}, -r_{31})^t = \eta l_2^*, \qquad \eta \in \mathbf{R}\end{aligned} \tag{19}$$

such that

$$\|l_1\| = 1, \qquad \|l_2\| = 1, \qquad l_1 \perp l_1^*, \qquad l_2 \perp l_2^*. \tag{20}$$

All mappings between any four noncoplanar points of the two sets are possible by a rigid, one-parameter family of motions under the weak perspective model. The principal 2×2 minor R^* of R can be written as

$$R^* = (l_1 l_1^*) \begin{pmatrix} -\sqrt{1-\eta^2}\, l_2' \\ l_2'^{\perp} \end{pmatrix}, \qquad -1 \le \eta \le 1, \tag{21}$$

yielding

$$R = \begin{bmatrix} R^* & \eta l_1 \\ \eta l_2' & r_{33} \end{bmatrix}. \tag{22}$$

With the four known correspondences (0,0), $(\mathbf{p}_2, \mathbf{p}_2')$, $(\mathbf{p}_3, \mathbf{p}_3')$, and $(\mathbf{p}_4, \mathbf{p}_4')$ the basic mapping $\mathbf{f}$ is defined as

$$\mathbf{f}(c_1\mathbf{p}_2 + c_2\mathbf{p}_3) = c_1\mathbf{f}(\mathbf{p}_2) + c_2\mathbf{f}(\mathbf{p}_3), \qquad \mathbf{f}(\mathbf{p}_2) = \mathbf{p}_2' \wedge \mathbf{f}(\mathbf{p}_3) = \mathbf{p}_3' \tag{23}$$

for $c_1, c_2 \in \mathbf{R}$ and where $(\mathbf{p}_2, \mathbf{p}_3)$ forms a basis in $\mathbf{R}^2$. A sufficient and necessary condition for points 0, $\mathbf{p}_2$, $\mathbf{p}_3$, and $\mathbf{p}_4$ to be noncoplanar is that $\mathbf{f}(\mathbf{p}_4) \neq 0$. A necessary condition for a point $\mathbf{p}_j'$ to be a correspondence of $\mathbf{p}_i$ is that it lie on the line λ_i that passes through $\mathbf{f}(\mathbf{p}_i)$ and has direction l_1. Now the scale s is recovered uniquely from $\mathbf{p}_2 \cdot l_1^* = s\, \mathbf{p}_2 \cdot l_2^*$, and the matching direction l_1 is determined by $\mathbf{f}(\mathbf{p}_4) - \mathbf{p}_4'$. Now the epipolar distance is given by

$$d(\mathbf{p}_j', \lambda_i) = |\, l_1^* \cdot \mathbf{s}_j - l_1^* \cdot \mathbf{f}(\mathbf{p}_i)|. \tag{24}$$

REFERENCES

Aloimonos, L., and C. M. Brown. 1986. Perception of structure from motion. *Proc. IEEE Conf. Computer Vision and Pattern Recognition*, pp. 22–26.

Baigent, C. L., and G. Müller. 1990. Carbon-based immunocytochemistry. A new approach to the immunostaining of epoxy-resin-embedded material. *J. Microsc.* 158:73–80.

Barnard, S. T. 1987. Stereo matching by hierarchical microchannel annealing. Technical note 414. SRI International.

Barnard, S. T. 1986. A stochastic approach to stereo vision. *Proc. 5th Inst. Conf. on Artificial Intelligence.* 1:676–680.

Bonnet, N., C. Quintana, P. Favard, and N. Favard. 1985. Three-dimensional graphical reconstruction from HVEM stereoviews of biological specimens by means of a microcomputer. *Biol. Cell.* 55:125–138.

Borgefors, G. 1986. Distance transformations in digital images. *Computer Vision Graph. Image Process.* 34:344–371.

Boyer, K. L., and A. C. Kak. 1988. Structural stereopsis for 3D vision. *IEEE Trans. Pattern Anal. Machine Intell.* 10:144–166.

Bron, Cph., Ph. Gremillet, D. Launy, M. Jourlin, H. P. Gautschi, Th. Bächi, and J. Schüpbach. 1990. Three-dimensional electron microscopy of entire cells. *J. Microsc.* 157:115–126.

Burry, R. W., J. J. Lah, and D. M. Hayes. 1992. GAP-43 distribution is correlated with development of growth cones and presynaptic terminals. *J. Neurocytol.* 21:413–425.

Carnevali, P., L. Coletti, and S. Patarnello. 1985. Image processing by simulated annealing. *IBM J. Res. Dev.* 29:569–579.

Černý, V. 1985. Thermodynamical approach to the traveling salesman problem: an efficient simulation algorithm. *J. Optim. Theory Appl.* 45:41–51.

Danscher, G. 1981. Localization of gold in biological tissue. *Histochemistry.* 71:81–88.

de Graaf, A., P. M. P. van Bergen en Henegouwen, A. M. L. Meijne, R. van Driel, A. J. Verkleij. 1991. Ultrastructural localization of nuclear matrix proteins in HeLa cells using silver-enhanced ultra-small gold probes. *J. Histochem. Cytochem.* 39:1035–1045.

Downes, C. S., G. H. Leno, and R. A. Laskey. 1992. The nuclear membrane prevents replication of human G2 nuclei but not G1 nuclei in Xenopus egg extract. *Cell.* 69:151–158.

El Gamal, A. A., L. A. Hemachandra, I. Shperling, and V. K. Wei. 1987. Using simulated annealing to design good codes. *IEEE Trans. Inform. Theory.* 33:116–123.

Elias, H. 1971. Three-dimensional structure identified from single sections: misinterpretation of flat images can lead to perpetuated errors. *Science.* 174:993–1000.

Fey, E. G., G. Krochmalnic, S. Penman. 1986. The nonchromatin substructures of the nucleus: the ribonucleoprotein (RNP)-containing and RNP-depleted matrices analyzed by sequential fractionation and resinless section electron microscopy. *J. Cell Biol.* 102:1654–1665.

Geman, S., and D. Geman. 1984. Stochastic relaxation, Gibbs distributions, and the Bayssian restoration of images. *IEEE Trans. Pattern Anal. Machine Intell.* 6:721–741.

Geraud, G., A. Soyer, and Y. Epelboin. 1988. Three-dimensional computer reconstruction from serial sections of cell nuclei. *Biol. Cell.* 62:111–117.

Gonzales, R. C., and P. Wints. 1987. Digital Image Processing. Addison-Wesley, Reading, MA.

Hajek, B. 1988. Cooling schedules for optimal annealing. *Math. Oper. Res.* 13:311–329.

Hoppe, W., and R. Heger. 1980. Three-dimensional structure determination by electron microscopy (non-periodic specimens). *In* Computer Processing of Electron Microscope Images. P. W. Hawkes, editor. Springer-Verlag, Berlin. 127–185.

Horisberger, M. 1992. Colloidal gold and its application in cell biology. *Int. Rev. Cytol.* 136:227–287.

Huang, T. S., and C. H. Lee. 1989. Motion and structure from orthographic projections. *IEEE Trans. Pattern Anal. Machine Intell.* 11:536–540.

Humbel, B., and M. Müller. 1986. Freeze-substitution and low temperature embedding. *In* Science of Biological Specimen Preparation, 1985. M. Müller, R. P. Becker, A. Boyde, and J. J. Wolosewick, editors. AMF, O'Hare, IL.

Hummel, R. A., and S. W. Zucker. 1983. On the foundations of relaxation labeling processes. *IEEE Trans. Pattern Anal. Machine Intell.* 5:267–287.

Immi, M. 1991. A noise peak elimination filter. *CVGIP: Graph. Models Image Process.* 53:204–211.

King, M. V. 1981. Theory of stereopsis. *In* Methods in Cell Biology, Vol. 22. J. N. Turner, editor. Academic Press, New York. 13–32.

Kirkpatrick, S., C. D. Gelatt, and M. P. Vecchi. 1983. Optimization by simulated annealing. *Science.* 220:671–680.

Krijnse-Locker, J., M. Ericsson, P. J. M. Rottler, and G. Griffiths. 1994. Characterization of the budding compartment of mouse hepatitis virus: evidence that transport from the RER to the Golgi complex requires only one vesicular transport step. *J. Cell Biol.* 124:55–70.

Lee, C. H., and T. S. Huang. 1990. Finding point correspondences and determining motion of a rigid object from two weak perspective views. *Computer Vision Graph. Image Process.* 52:309–327.

Lee, J. S. L., R. M. Haralick, and L. S. Shapiro. 1986. Morphologic edge detection. *Proc. 8th Int. Conf. Pattern Recognition,* pp. 369–373.

Lemmens, M. J. P. M. 1988. A survey of matching techniques. *Commun. V of the ISPRS Congress,* pp. 1–13.

Leunissen, J. L. M., P. F. E. M. van der Plas, and P. E. J. Borghgraaf. 1989. AuroProne One: a new and universal ultra small gold particle based (immuno) detection system for high sensitivity and improved penetration. *In* Sciences, Vol. 1. J. Life, editor. AuroFile.

Levinthal, C. 1984. The formation of three-dimensional biological structures: computers uses and future needs. *Ann. N.Y. Acad. Sci.* 426:171–180.

Lookeren-Campagne, M. van, C. G. Dotti, E. R. S. Jap Tjoan San, A. J. Verkleij, W. H. Gispen, and A. B. Oestreicher. 1992. B-50/GAP 43 localization in polarized hippocampal neurons in vitro: an ultrastructural quantitative study. *Neuroscience.* 50:35–52.

Luther, P. K., M. C. Lawrence, and R. A. Crowther. 1988. A method for monitoring the collapse of plastic sections as a function of electron dose. *Ultramicroscopy.* 24:7–18.

Marr, D. 1979. Vision. Freeman and Co., New York.

Meiesner, D. M., and H. Schwars. 1990. Improved cryoprotection and freeze-substitution of embryonic quail retina: A TEM study on ultrastructural preservation. *J. Electron. Microsc. Tech.* 14:348–356.

Metropolis, N., A. Rosenbluth, M. Rosenbluth, A. Teller, and E. Teller. 1953. Equation of state calculations by fast computing machines. *J. Chem. Phys.* 21:1087–1092.

Moss, V. A., D. McEwan-Jenkinson, and H. Y. Elder. 1990. Automated image segmentation and serial section reconstruction in microscopy. *J. Microsc.* 158:187–196.

Nickerson, J. A., G. Krockmalnic, D. He, and S. Penman. 1990. Immunolocalization in three dimensions: immunogold staining of cytoskeleton and nuclear matrix proteins in resinless electron microscopy sections.

Proc. Natl. Acad. Sci. USA. 87:2259–2263.

O'Gorman, L., and A. C. Sanderson. 1984. The convergent squares algorithm: An efficient method for locating peaks in multidimensions. *IEEE Trans. Pattern Anal. Machine Intell.* 6:280–287.

Otha, Y., and T. Kanade. 1985. Stereo by intra- and inter-scanline search using dynamic programming. *IEEE Trans. Pattern Anal. Machine Intell.* 7:139–154.

Otten, M. T., D. J. Stensel, D. R. Cousens, B. M. Humbel, J. L. M. Leunissen, Y. D. Stierhof, and W. M. Busing. 1992. High-angle annular dark-field STEM imaging of immunogold labels. Scanning. 14:282–289.

Pavlidis, T., and Y. T. Liow. 1990. Integrating region growing and edge detection. *IEEE Trans. Pattern Anal. Machine Intell.* 12:225–233.

Peachly, L. D. 1986. The extraction of three-dimensional information from stereo micrographs of thick sections using computer graphics methods. *In* Recent Advances in Electron and Light Optical Imaging in Biology and Medicine. New York Academy of Science, New York.

Perkins, W. J., and R. J. Green. 1982. Three-dimensional reconstruction of biological sections. *J. Biomed. Eng.* 4:37–43.

Provencher, S. W., and R. H. Vogel. 1988. Three-dimensional reconstruction from electron micrographs of disordered specimens. *Ultramicroscopy.* 25:209–222.

Shapiro, L. G., and R. M. Haralick. 1981. Structural descriptions and inexact graph matching. *IEEE Trans. Pattern Anal. Machine Intell.* 3:504–519.

Shaw, P. J., D. A. Agard, Y. Hiraoka, and J. W. Sedat. 1989. Tilted view reconstruction in optical microscopy: three-dimensional reconstruction of *Drosophila melagaster* embryo nuclei. *Biophys. J.* 55:101–110.

Skoglund, U. 1992. An overview of the electron microscope tomography method. *In* Electron Microscopy 92. A. Ríos, editor. Secretariado de Publicaciones de la Universidad de Granada, Granada, Spain, for EUREM-92. 465–467.

Starink, J. P. P. 1993. Analysis of electron microscope images: 3-D localization of immuno-markers. Ph.D. thesis. Delft University of Technology, Delft, The Netherlands.

Starink, J. P. P. 1995. Finding point correspondences using simulated annealing. *Pattern Recognition.* 28:231–240.

Starink, J. P. P., and I. T. Young. 1993. Localization of circular objects. Pattern Recognition Lett. 14:905–906.

Stierhof, Y. D., B. M. Humbel, R. Homann, M. T. Otten, and H. Schwars. 1992. Direct visualization and silver enhancement of ultra-small gold tagged antibodies on immunolabelled ultrathin resin sections. *Scanning Microsc.* 6:1009–1022.

Tan, H. L., and S. B. Gelfland. 1992. A cost minimization approach to edge detection using simulated annealing. *IEEE Trans. Pattern Anal. Machine Intell.* 14:3–18.

Ullman, S. 1979. The Interpretation of Visual Motion. MIT Press, Cambridge, MA.

Venot, A., J. F. Lebruchec, and J. C. Roucayrol. 1984. A new class of similarity measures for robust image registration. *Computer Vision Graph. Image Process.* 28:176–184.

Verbeck, P. W., H. A. Vrooman, and L. J. van Vliet. 1988. Low level image processing by max–min filters. *Signal Process.* 15:249–258.

Vetterling, W. T., S. A. Teukolsky, W. H. Press, and B. P. Flannery. 1993. Numerical Recipes. Cambridge University Press, Cambridge, UK.

Zucker, S. W. 1976. Survey region growing: childhood and adolescence. *Computer Graph. Image Process.* 5:382–399.